p–MoO3 Nanostructures/n–TiO2 Nanofiber Heterojunctions: Controlled Fabrication and Enhanced Photocatalytic Properties

9 AUTHORS, INCLUDING:

Kexin Wang
Northeast Normal University
10 PUBLICATIONS **66** CITATIONS

SEE PROFILE

Xin Zhang
Northeast Normal University
17 PUBLICATIONS **250** CITATIONS

SEE PROFILE

Peng Zhang
Northeast Normal University
31 PUBLICATIONS **1,329** CITATIONS

SEE PROFILE

Mingyi Zhang
Harbin Normal University
**60** PUBLICATIONS **1,776** CITATIONS

SEE PROFILE

p-MoO3 Nanostructures/n-TiO2 Nanofiber Heterojunctions: Controlled Fabrication and Enhanced Photocatalytic Properties

Mingxing Lu,[†] Changlu Shao,*[,†] Kexin Wang,[†] Na Lu,[†] Xin Zhang,[†] Peng Zhang,[†] Mingyi Zhang,[†] Xinghua Li,*[,†] and Yichun Liu[†]

[†]Center for Advanced Optoelectronic Functional Materials Research, and Key Laboratory of UV Light-Emitting Materials and Technology of Ministry of Education, Northeast Normal University, 5268 Renmin Street, Changchun 130024, People's Republic of China

ABSTRACT: In this work, p-MoO3 nanostructures/n-TiO2 nanofiber heterojunctions (p-MoO3/n-TiO2−NF-HJs) were obtained by a two-step fabrication route. First, MoO2 nanostructures were hydrothermally grown on electrospun TiO2 nanofibers. Second, by thermal treatment of the obtained MoO2 nanostructures/TiO2 nanofibers, p-MoO3/n-TiO2−NF-HJs were obtained due to the phase transition of MoO2 to MoO3. With increasing the concentration of molybdenum precursor in hydrothermal process, the morphologies of MoO2 changed from nanoparticles to nanosheets, and then fully covered shells with an increased loading on TiO2 nanofibers. After calcination, the obtained p-MoO3/n-TiO2−NF-HJs possessed similar morphology to that without thermal treatment. X-ray photoelectron spectra showed that both Ti 2p and O_{Ti-O} 1s peaks of p-MoO3/n-TiO2−NF-HJs shifted to higher binding energies than that of TiO2 nanofibers, suggesting electron transfer from TiO2 to MoO3 in the formation of p−n nanoheterojunctions. The p−n nanoheterojunctions decreased photoluminescence intensity, suppressed photogenerated electrons and holes recombinations, and enhanced charge separation and photocatalytic efficiencies. The apparent first-order rate constant for the degradation of RB by p-MoO3/n-TiO2−NF-HJs with nanosheets surface morphology was two times that of TiO2 nanofibers. For the core/shell structure of p-MoO3/n-TiO2−NF-HJs, the internal electric field of p−n junction forced the photogenerated electrons transferring to TiO2 cores, then decreased the surface photocatalytic reactions and led to the lowest photocatalytic activity among the p-MoO3/n-TiO2−NF-HJs.

KEYWORDS: MoO3, TiO2, nanofibers, heterojunction, photocatalysis, electrospinning
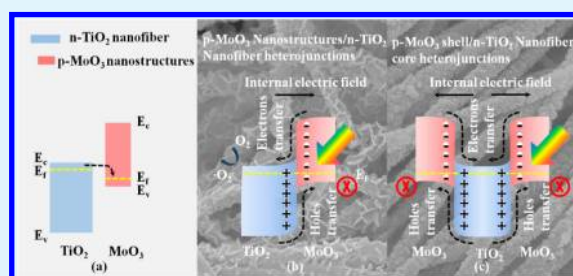
1. INTRODUCTION

In recent years, the design and construction of semiconductor photocatalysts have been extensively studied due to the strong demand for degradation of various kinds of organic and inorganic pollutants to improve the environment.[1−7] As well-known n-type semiconductor photocatalysts, TiO2 nanostructures have attracted great amounts of attention due to their relatively high photocatalytic activity, biological and chemical stability, low cost, nontoxic nature, and long-term stability.[8−10] To enhance their photocatalytic activity, constructing heterojunctions of TiO2 nanostructures is usually taken as a general method to increase the electron−hole pair separation efficiency. Therefore, a large number of heterostructural nanomaterials, such as SnO2—TiO2, ZnO—TiO2, Bi2MoO6—TiO2, etc.,[11−13] have been investigated for many photocatalytic reactions. Theoretically, the formation of p−n heterojunctions could hinder the recombination of photogenerated electron−hole pairs more effectively and improve the photocatalytic activity. Previously, our group has reported that p-type NiO/n-type ZnO heterojunction nanofibers exhibited higher photocatalytic activity than the pure NiO and ZnO nanofibers for the degradation of RB dye under UV light irradiation due to the enhanced separation efficiency of photogenerated electron−hole pairs from the p−n heterojunctions.[14] Thus, it is a good idea to construct p−n heterojunctions of TiO2 nanocatalysts to enhance their photocatalytic activity and promote their industrial applications.[15−19]

MoO3 is a well-known p-type metal oxide semiconductor with high work function and good hole conductivity, which make it widely used in organic solar cells and organic light-emitting diodes.[20,21] The conduction and valence band position of MoO3 are both higher than that of TiO2.[22,23] Therefore, constructing p-MoO3/n-TiO2 heterojunctions might enhance the photocatalytic activity by hindering the charge recombination and improving the charge transfer process. However, very few studies have been performed on MoO3/TiO2 heterostructures for photocatalytic applications.[24−27] Agarwal et al. reported that using MoO3 as cocatalyst in TiO2 nanotubes (prepared by electrochemical anodization of Ti−Mo substrates with different Mo contents) can yield a strongly enhanced photocatalytic activity compared with pure TiO2 nanotubes.[27]

Table 1. Experimental Conditions, Morphology of MoO$_3$ Nanostructures, and the Atom Ratios of Ti, O, and Mo^a

samples	A (mM)	B (mM)	T_G (°C)	T_C (°C)	MP	Ti (At %)	O (At %)	Mo (At %)	Mo/Ti (R_c)
TM1	0.2	0.8	160		NPs	29.03	67.74	3.23	1:8.99
TM2	0.4	1.6	160		NSs	27.20	66.70	6.10	2:9.05
TM3	0.8	3.2	160		NPs	23.07	66.63	10.3	4:8.96
TM1-350	0.2	0.8	160	350	NPs	18.36	79.60	2.04	1:9.00
TM2-350	0.4	1.6	160	350	NSs	25.71	68.58	5.71	2:9.01
TM3-350	0.8	3.2	160	350	NPs	20.93	69.76	9.31	4:8.99
MoO$_3$ NPs	0.2	0.8	160	350	NPs				

^{a}A is (NH$_4$)$_6$Mo$_7$O$_{24}$·4H$_2$O; B is C$_4$H$_6$O$_6$; T_G is the hydrothermal temperature; T_C is the calcined temperature; The morphology of of MoO$_3$ (MP) is characterized by SEM (NPs and NSs were represented nanoparticles and nanosheets, respectively); Atom ratios of Ti, O, and Mo are determined by EDX, and the ratios of Mo to Ti atoms are calculated as R_c given in the last column.

But the p−n junction effect has not been considered and investigated in their reports.

Moreover, the structure and morphology of photocatalysts also have a strong effect on their photocatalytic activities. Among various morphologies, electrospun TiO$_2$ nanofibers have attracted great attention for their improved performance because of the following advantages: (1) the nanofibers possess a high surface-to-volume ratio which would be beneficial to adsorb a large amount of chemicals for photochemical reactions; (2) the one-dimensional (1D) nanostructure could provide quick charge transfer channels for the separation of photogenerated electron−hole pairs; (3) the unique three-dimensional (3D) porous structure makes it use light better through strong light scatterings; (4) the nonwoven nanofibrous web structure results in an easy separation from fluid by sedimentation.[28−30] To the best of our knowledge, there has been no report on the preparation and photocatalytic properties of 1D heterostructural MoO$_3$/TiO$_2$ nanofibers, which might possess high photocatalytic activity and favorable recycling characteristics.

On the basis of the above considerations, we attempt to construct a novel p-MoO$_3$ nanostructures/n-TiO$_2$ nanofiber heterojunctions (p-MoO$_3$/n-TiO$_2$−NF-HJs) by using electrospun TiO$_2$ nanofibers as hard templates. After the hydrothermal process, MoO$_2$ nanostructures are uniformly grown on TiO$_2$ nanofibers due to their 3D open structure and large surface areas, which could provide more active sites for the assembly of secondary nanostructures. The following thermal treatment results phase transition from MoO$_2$ to MoO$_3$, while the morphology of the heterostructure nanofibers is kept. The charge transfer of the p−n junction effect has been investigated by X-ray photoelectron spectra. The p-MoO$_3$/n-TiO$_2$−NF-HJs exhibit excellent photocatalytic activity compared with pure TiO$_2$ nanofiber and MoO$_3$ nanoparticles. Moreover, the morphology and loading amount of MoO$_3$ nanostructures also have an obviously effect on the photocatalytic properties of 1D p-MoO$_3$/n-TiO$_2$−NF-HJs.

2. EXPERIMENTAL SECTION

2. 1. Preparation of TiO$_2$ Nanofibers. First, 2 g of poly-(vinylpyrrolidone) powder (PVP, M_w = 1 300 000) was added to a mixture of 9 mL of absolute ethanol and 5 mL of acetic acid in a capped bottle. The obtained solution was stirred for 1 h to generate a homogeneous solution. Then, 2.0 g of Ti(OC$_4$H$_9$)$_4$ was added to the above solution, and the mixture was continuously stirred for another 1 h to make the precursor solution. For the electrospinning process, 3 mL of the precursor solution was placed in a 5 mL syringe which was equipped with a metal needle of 0.8 mm outer diameter and 0.6 mm inner diameter. A stainless steel plate covered with a sheet of aluminum foil was employed as the collector. The distance between

the needle tip and collector was about 15 cm, and the applied voltage was 9 kV. The as-collected nanofibers were calcined at 550 °C for 2 h to form anatase TiO$_2$ nanofibers (denoted as TM0 in the following discussion).

2.2. Fabrication of p-MoO$_3$/n-TiO$_2$−NF-HJs. In a typical experiment, 0.2 mmol of (NH$_4$)$_6$Mo$_7$O$_{24}$·4H$_2$O and 0.8 mmol of C$_4$H$_6$O$_6$ were dissolved in 16 mL of H$_2$O under magnetic stirring. The pH value of the solution was adjusted to 1 by 2 mol·L^{-1} HNO$_3$ solution. The resulting solution and 20 mg of TiO$_2$ nanofibers were transferred into a 20 mL Teflon-lined stainless autoclave, sealed and maintained at 160 °C for 5 h, and then cooled down to room temperature. The as-fabricated products were collected, washed several times with ethanol and deionized water, respectively, and then dried at 60 °C for 12 h. Then, MoO$_2$ nanostructures/TiO$_2$ nanofibers heterojunctions (TiO$_2$−MoO$_2$) were fabricated, which was denoted as TM1. By this method, TM2 and TM3 were prepared by increasing the additive amount of (NH$_4$)$_6$Mo$_7$O$_{24}$·4H$_2$O and C$_4$H$_6$O$_6$. Then, three samples of p-MoO$_3$/n-TiO$_2$−NF-HJs were fabricated by annealing TM1, TM2, and TM3 in muffle furnace at 350 °C for 3 h and denoted as TM1-350, TM2-350, and TM3-350, respectively. For comparison, pure MoO$_3$ nanoparticles were obtained and denoted as MoO$_3$ NPs by the same process for preparation of p-MoO$_3$/n-TiO$_2$−NF-HJs in the absence of TiO$_2$ nanofibers. The detailed experimental conditions and the characteristics of MoO$_2$ and MoO$_3$ nanostructures are listed in Table 1.

2.3. Characterization. X-ray diffraction (XRD) measurements were carried out using a D/max 2500 XRD spectrometer (Rigaku) with Cu Kα line of 0.1541 nm. Scanning electron microscopy (SEM; Quanta 250 FEG) and transmission electron microscopy (TEM; JEOL JEM-2100) were used to characterize the morphologies of the products. Energy dispersive X-ray (EDX) spectroscopy being attached to SEM was used to analyze the composition of samples. X-ray photoelectron spectroscopy (XPS) was performed on a VG-ESCALAB LKII instrument with Mg Kα ADES ($h\nu$ = 1253.6 eV) source at a residual gas pressure of below 1 × 10^{-8} Pa. UV−vis diffuse reflectance (DR) spectroscopy of the samples were recorded on a Cary 500 UV−vis-NIR spectrophotometer with the wavelengths from 200 to 800 nm. Photoluminescence (PL) spectra of the samples were detected with a Jobin Yvon HR800 micro-Raman spectrometer using a 325 nm line from a He−Cd laser.

2.3. Photocatalytic Test. The photoreactor was designed with an internal light source (50 W high pressure mercury lamp with main emission wavelength 313 nm and an average light intensity of 2.85 mW·cm^{-2}) surrounded by a water-cooling quartz jacket to cool the lamp. 100 mL of RB solution (~10 mg·L^{-1}) with 0.01 g photocatalyst was stirred in the dark for 30 min to obtain a good dispersion and reach adsorption−desorption equilibrium between the organic molecules and the catalyst surface. Decreases in the concentrations of dyes were analyzed by a Cary 500 UV−vis-NIR spectrophotometer at λ = 554 nm. At given intervals of illumination, samples of the reaction solution were taken out and analyzed.

3. RESULTS AND DISCUSSION

3.1. Structure and Morphology. The XRD patterns of TiO_2 nanofibers (TM0), TiO_2/MoO_2-1 (TM1), and TM1 calcinated at 250 °C (TM1-250) and 350 °C (TM1-350), as well as MoO_3 NPs are shown in Figure 1(a). The diffraction
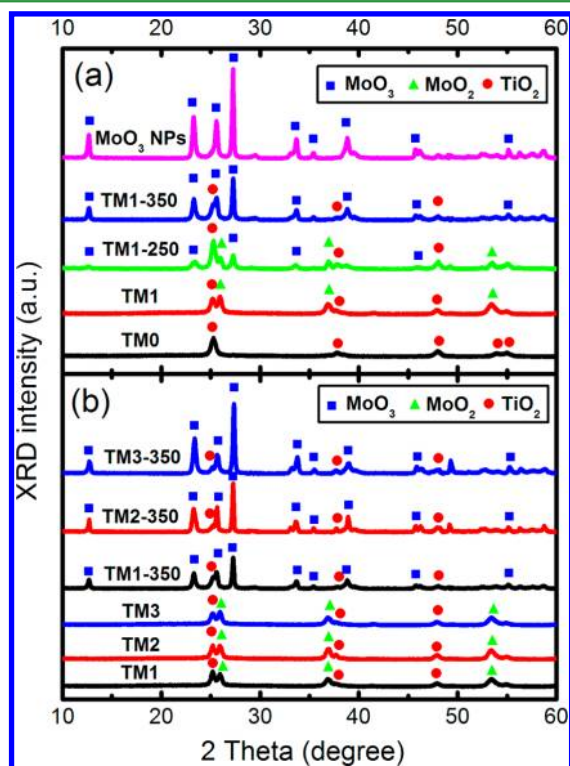

Figure 1. (a) XRD patterns of TiO_2 nanofibers (TM0), TiO_2/MoO_2-1 (TM1), TM1 calcined at 250 °C (TM1-250) and 350 °C (TM1-350), and MoO_3 nanoparticles (MoO_3 NPs); (b) XRD patterns of TiO_2/MoO_2-1 (TM1), TiO_2/MoO_2-2 (TM2), TiO_2/MoO_2-3 (TM3), and the corresponding XRD patterns for the three samples after calcination at 350 °C (denoted as TM1-350, TM2-350, and TM3-350).

peaks of TM0 at about 2θ = 25.3°, 37.8°, 48.0°, 54.0°, and 54.9° could be perfectly indexed to the diffractions of (101), (004), (200), (105), and (211) crystal faces of anatase TiO_2 (PDF card: 21-1272, JCPDS), respectively. The XRD pattern of pure MoO_3 NPs, corresponded to the orthorhombic phase of MoO_3 (PDF card: 5-506, JCPDS), is also given for comparison. For TM1 obtained after hydrothermal reaction, three additional diffraction peaks with 2θ values of 26.0°, 37.1°, and 53.5° could be observed. They could be perfectly indexed to the diffractions of (011), (200), and (022) crystal planes of the tetragonal MoO_2 crystalline phase (PDF card: 2-422, JCPDS). After calcination at 250 °C, the diffraction peaks of TM1-250 corresponding to (020), (110), (021), (111), and (200) crystal planes of orthorhombic phase of MoO_3 could be observed at 2θ values of 12.8°, 23.3°, 27.5°, 33.6°, and 46.1°. It suggests that there is a phase transformation from a tetragonal MoO_2 to a more stable orthorhombic MoO_3 phase after the calcination process. With increasing the calcination temperature to 350 °C, the diffraction peaks of tetragonal MoO_2 fully disappeared, indicating a complete phase transformation to orthorhombic MoO_3 for TM1-350. Therefore, only MoO_3 and TiO_2 form in TM1-350 and no anatase-to-rutile phase transition occurs during the synthesis of p-MoO_3/n-TiO_2−NF-HJs. Figure 1(b) represents XRD patterns of TiO_2/MoO_2-

1 (TM1), TiO_2/MoO_2-2 (TM2), TiO_2/MoO_2-3 (TM3), as well as the corresponding XRD patterns for the three samples after calcination at 350 °C (denoted as TM1-350, TM2-350, and TM3-350). The ratio of diffraction peaks intensity for MoO_3 to TiO_2 is increased with increasing the concentration of molybdenum precursor in hydrothermal process, suggesting that p-MoO_3/n-TiO_2−NF-HJs with different amount of MoO_3 loading have been successfully prepared after thermal treatment at 350 °C.

The morphologies of the samples are investigated by SEM technology. Before hydrothermal reactions, TiO_2 nanofibers with diameters ranging from 200 to 400 nm exhibit smooth surfaces and ultralong lengths, which are shown Figure 2(a).
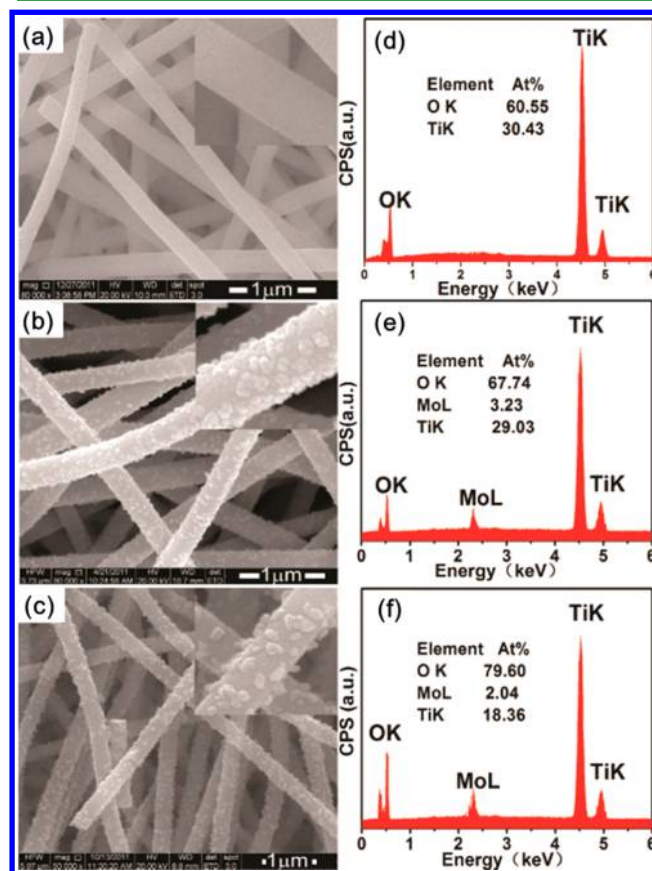

Figure 2. SEM images of (a) TiO_2 nanofibers (TM0), (b) TiO_2/MoO_2-1 (TM1), (c) TM1 calcined at 350 °C (denoted as TM1-350), and EDX spectra of (d) TM0, (e) TM1, and (f) TM1-350.

After the hydrothermal process, MoO_2 nanoparticles are uniformly distributed across the surface of each fiber without aggregation, offering high level exposure of the nanoparticles' surface, as shown in Figure 2(b). The EDX spectrum of Figure 2(e) also indicates that MoO_2 nanoparticles have been grown on TiO_2 nanofibers. After calcination at 350 °C, the morphology does not change significantly, while the oxygen content is increased from 67.74 At% for TM1 in Figure 2 (e) to 79.60 At% for TM1-350 in Figure 2(f), which gives another evidence for the phase transformation from MoO_2 to MoO_3.

By simply changing the experimental parameters, the secondary MoO_2 nanostructures grown on TiO_2 nanofibers could be further controlled with different morphologies and loading amounts. When the amount of $(NH_4)_6Mo_7O_{24}\cdot4H_2O$ is increased from 0.2 mmol (for TM1) to 0.4 mmol (for TM2),
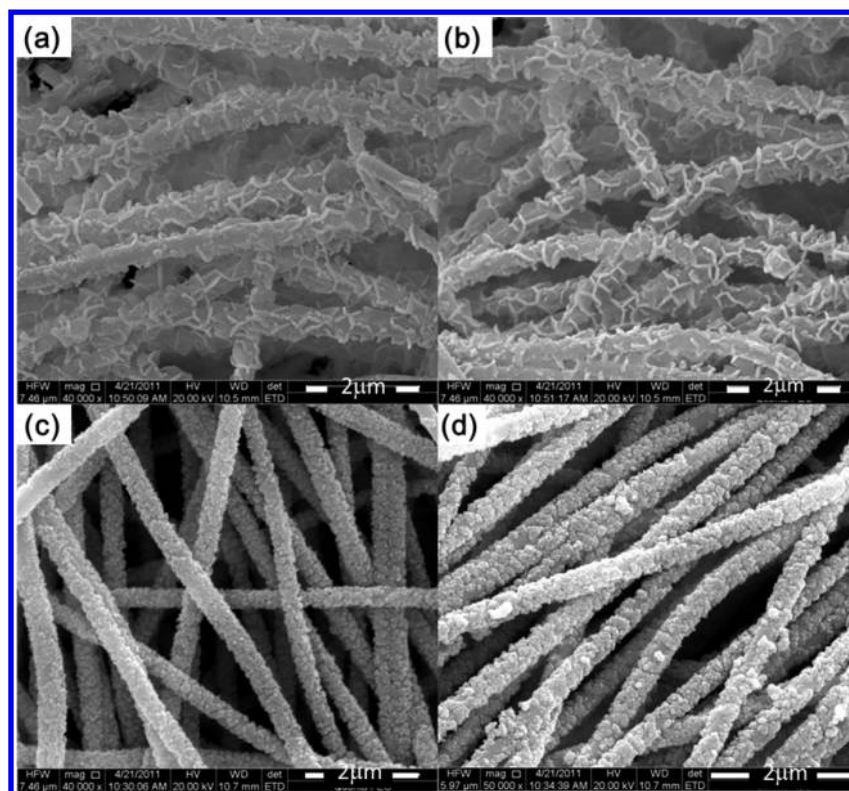
Figure 3. SEM images of (a) TiO_2/MoO_2-2 (TM2), (c) TiO_2/MoO_2-3 (TM3), and SEM images of the corresponding samples after calcination at 350 °C, denoted as TM2-350 (b) and TM3-350 (d), respectively.
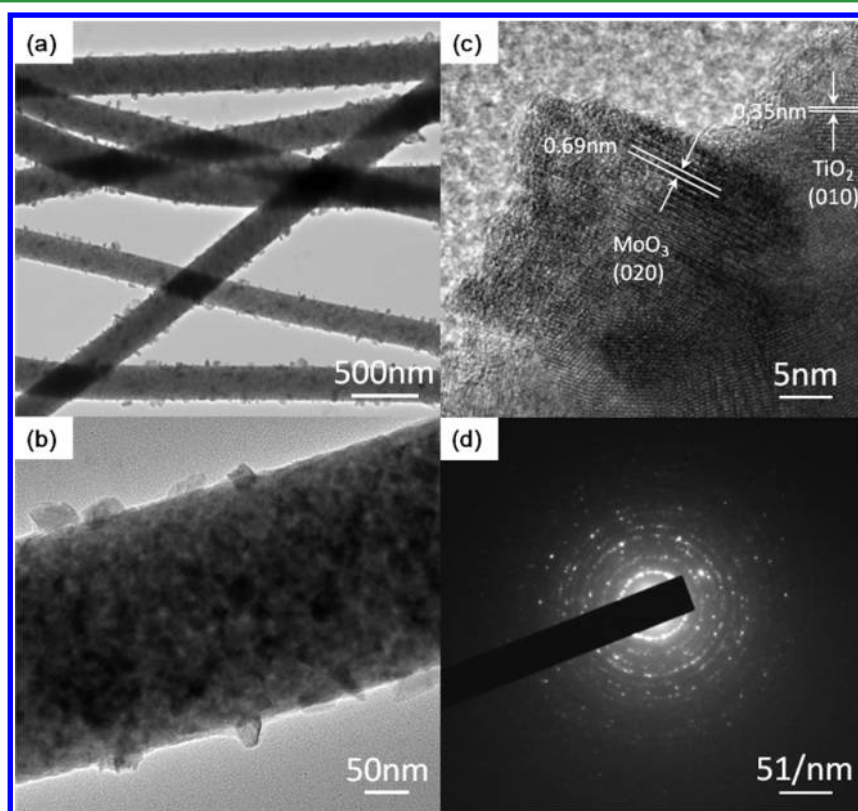

Figure 4. (a),(b) TEM image of sample TiO_2/MoO_2-1 after calcination at 350 °C (TM1-350); (c) HRTEM; and (d) SAED of TM1-350.

the morphology of the secondary MoO_2 nanostructures significantly changes from well-dispersed nanoparticles to uniform nanosheets, as shown in Figure 3(a). However, when

the additive amount of $(NH_4)_6Mo_7O_{24}·4H_2O$ is increased to 0.8 mmol, the density of the nanoparticles in Figure 3(c) is dramatically increased, forming nearly core/shell structures. It

is worth pointing out that the high porosity and large surface area of TiO_2 nanofibers are advantageous for uniform growth and distribution of MoO_2 nanostructures on the surface of TiO_2 nanofibers.[31] Moreover, after thermal treatment, the morphologies of the MoO_2 nanostructures are well retained, with fully transformed to MoO_3 nanostructures, as shown in Figure 3(b),(d). The morphologies might also have a strong effect on the photocatalytic properties, which would be discussed in the following section. Furthermore, the atom ratios of Ti, O, and Mo calculated from the EDX spectra (not shown) are given in Table 1. The ratios of Mo to Ti atoms are very close to 1:9, 2:9, and 4:9 for TM1, TM2, and TM3, respectively, indicating that only phase transformation occurred. Given the XRD results, the morphology and composition both indicate that p-MoO_3/n-TiO_2−NF-HJs with different amount of MoO_3 loading have been successfully prepared after thermal treatment at 350 °C.

Figure 4(a),(b) gives the typical TEM images of TM1-350. It could be clearly observed that MoO_3 nanoparticles are uniformly grown on the surface of TiO_2 nanofibers. The HRTEM image displays two types of clear lattice fringes as shown in Figure 4(c). One set of the fringe spacing is ca. 0.35 nm, corresponding to the (101) plane of anatase crystal structure of TiO_2. Another set of the fringe spacing is ca. 0.69 nm, which corresponds to the (020) lattice spacing of orthorhombic MoO_3. Selected-area electron diffraction (SAED) pattern in Figure 4(d) clearly demonstrates the polycrystal nature of MoO_3 nanoparticles.

3.2. X-ray Photoelectron Spectroscopy (XPS) Spectra.

XPS measurements are also performed to further investigate the chemical composition and interactions of p-MoO_3/n-TiO_2−NF-HJs. Fully scanned XPS spectra of TiO_2 nanofibers (TM0) and the sample of TiO_2/MoO_2-1 after calcination at 350 °C (TM1-350) in Figure 5(a) demonstrate that Ti, O, and C elements exist in TiO_2 nanofibers, while Ti, Mo, O, and C exist in TM1-350. The present of C element could be ascribed to the adventitious carbon-based contaminant, and the binding energy of C 1s peak at 284.6 eV is used as a reference for calibration. We clearly observe the peaks related to Mo 3d and 3p in the XPS spectrum of TM1-350 in Figure 5(a). The high resolution XPS spectrum of Mo 3d region around 234 eV is also shown in Figure 5(d). The peaks from Mo $3d_{5/2}$ and $3d_{3/2}$ are located at 232.4 and 235.6 eV, respectively, indicating that the chemical state of Mo is present as Mo^{6+} in TM1-350.[32,33] It further confirms that p-MoO_3/n-TiO_2−NF-HJs have been successfully prepared.

Moreover, the XPS spectra of Ti 2p and O 1s for TM0 and TM1-350 are also given in Figure 5(b),(c), respectively. The splitting between Ti $2p_{1/2}$ and Ti $2p_{3/2}$ are both 5.7 eV for TM0 and TM1-350, suggesting a normal state of Ti^{4+} in pure TiO_2 nanofibers and p-MoO_3/n-TiO_2−NF-HJs.[34,35] The binding energy of Ti $2p_{3/2}$ for TM1-350 locates at 458.7 eV, which is about 0.3 eV higher than that of TM0 (458.4 eV). For the O 1s spectrum, TM0 shows a wide and asymmetric peak, which contains more than one chemical states, including crystal lattice oxygen ($O_{Ti−O}$), surface hydroxyl groups (O_{OH}), and adsorbed water with increasing binding energy.[31] However, the O 1s peak for TM1-350 shifts to higher binding energy and becomes much broaden with a suppression of surface hydroxyl groups (O_{OH}) and adsorbed water. It could be fitted by two peaks located at 529.9 and 530.7 eV which correspond to $O_{Ti−O}$ and $O_{Mo−O}$, respectively. The binding energy of $O_{Ti−O}$ for TM1-350 is also higher than that of TM0, similar to the behavior of Ti 2p.

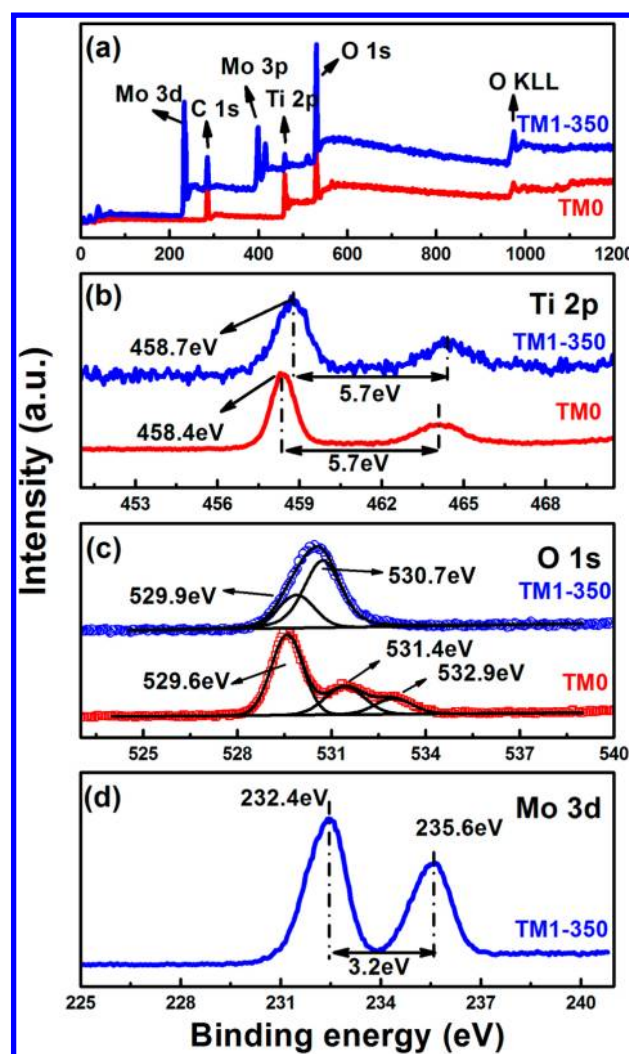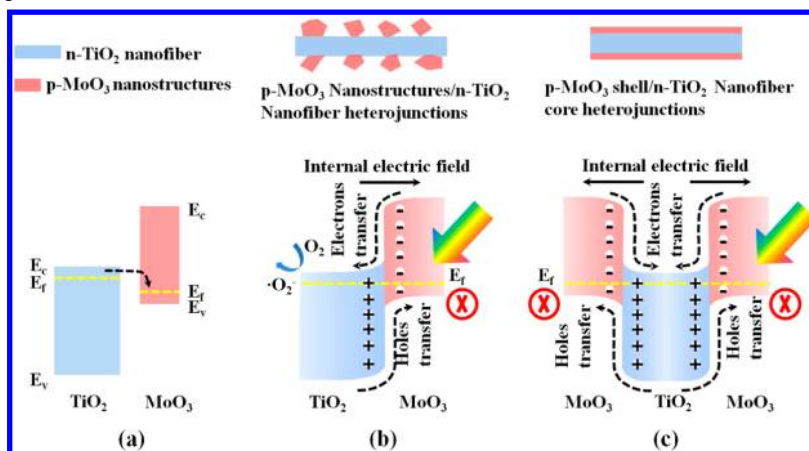**Figure 5.** XPS fully scanned spectra (a), XPS spectra of Ti 2p (b) and O 1s (c) for TiO_2 nanofibers (TM0) and sample TiO_2/MoO_2-1 after calcination at 350 °C (TM1-350); and XPS spectrum of Mo 3d (d) for TM1-350.

The increasing binding energies of Ti 2p and $O_{Ti−O}$ 1s could be explained by considering the electrons transfer from TiO_2 to MoO_3. As shown in Scheme 1(a), the conduction band of MoO_3 is higher than TiO_2, but its Fermi level is much lower than that of TiO_2 due to its high work function. When p-MoO_3 and n-TiO_2 contact with each other, electrons would transfer from TiO_2 to MoO_3, as indicated by the dashed line in Scheme 1(a), forming positively and negatively charged regions in TiO_2 and MoO_3, respectively, as illustrated in Scheme 1(b),(c). It is noted that the detected photoelectrons of TiO_2 in XPS measurements would be mainly from the surface layer (<10 nm), which is positively charged for TM1-350 due to the depletion of electrons. The positive potential would increase the binding energy of Ti and O simultaneously as represented in Figure 5(b),(c). In fact, our group had previously found that the binding energy of Zn 2p shifted toward higher binding energy when n-type ZnO contacted with p-type NiO forming p/n heterojunction nanofibers.[14] Recently, Chen et al. reported that the C 1s of epitaxial graphene (EG) also shifted to higher binding energy after coating with MoO_3 thin film, due to the electrons transfer from EG to MoO_3.[33] Hence, the binding energy shifts of Ti 2p and $O_{Ti−O}$ 1s could be attributed to the

Scheme 1. Energy Band Alignment of *p*-MoO₃ Nanostructures and *n*-TiO₂ Nanofiber Heterojunctions and the Postulate Mechanism for Photodegradation of RB under UV Irradiation[a]

[a](a) Before contact, the arrow with dashed line shows the direction of electron transfer if *p*-MoO₃ and *n*-TiO₂ contacts with each other; (b) after contact, the arrow with solid line gives the internal electric field in the heterojunction due to the electron transfer, the arrows with dashed lines indicate the electron and hole separation under light irradiation; and (c) the contacts with core/shell structures, the separated photoelectrons are confined in the inner cores and could not take part in the photocatalysis.

electron transfer from TiO₂ to MoO₃, resulting in positively charged surfaces. These results further confirm the formation of p−n nanoheterojunctions in *p*-MoO₃/*n*-TiO₂−NF-HJs.

3.3. Optical Properties. To investigate the light absorption properties of *p*-MoO₃/*n*-TiO₂−NF-HJs, diffuse reflectance spectra are presented in Figure 6. For comparison, the spectra
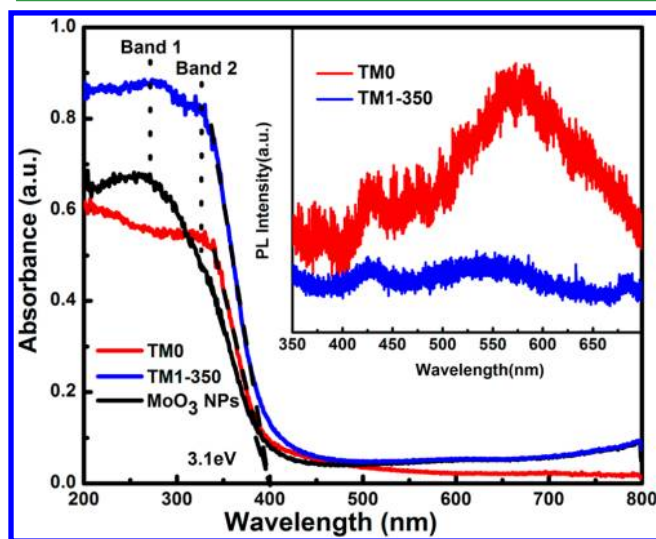

Figure 6. UV−vis diffuse reflectance spectra of TiO₂ nanofibers (TM0), sample TiO₂/MoO₂-1 after calcination at 350 °C (TM1-350), and MoO₃ NPs; the inset shows photoluminescence spectra of TM0 and TM1-350 excited by 325 nm laser.

of TiO₂ nanofibers and MoO₃ NPs are also plotted. The TiO₂ nanofibers show a clear absorption edge at about 400 nm with fundamental absorption in the UV region. For the sample TiO₂/MoO₂-1 after calcination at 350 °C (TM1-350), the absorption bands 1 and 2 could be assigned to the absorption of MoO₃ and TiO₂, respectively. Obviously, the light absorption ability of TM1-350 is enhanced compared with TM0 and MoO₃ NPs. Furthermore, the inset of Figure 6 shows PL spectra of TM0 and TM1-350 excited by 325 nm laser. The PL intensity is decreased evidently for TM1-350 after the

formation of *p*-MoO₃/*n*-TiO₂−NF-HJs, suggesting that the recombinations of photogenerated electrons and holes could be suppressed by forming p−n nanoheterojunctions.[14,34]

3.4. Photocatalytic Activity. The photocatalytic degradation of Rhodamine B (RB) is chosen as a model reaction to evaluate the photocatalytic activities of *p*-MoO₃/*n*-TiO₂−NF-HJs, with TiO₂ nanofibers and MoO₃ NPs used as photocatalytic references. The degradation efficiency is defined as C/C_0, where C and C_0 stand for the remnants and initial concentration of RB, respectively. Figure 7(a) shows the adsorption of RB over different catalysts under dark. The adsorption−desorption equilibrium of RB in the dark is established within 30 min. The adsorption is increased in the order of TM0, TM1-350, and TM2-350 with increasing the loading of MoO₃ in *p*-MoO₃/*n*-TiO₂−NF-HJs because the roughness of their surface is increased gradually. However, TM3-350 with the highest loading in the present study shows the lowest adsorption. The SEM results indicate that MoO₃ nanoparticles are fully covered on the surface of TiO₂ nanofibers forming core/shell structures. Therefore, the surface area of TM3-350 is obviously decreased. Figure 7(b) represents the photodegradation of RB over different catalysts against irradiation time under UV light. After 50 min of reaction, the photodegradation efficiencies of RB are about 35% and 82% for TM0 and MoO₃ NPs, respectively. For TM1-350, the photodegradation efficiency is increased to 90% after 50 min of reaction. For TM2-350, 97% of RB is photocatalytically degraded within 40 min. However, TM3-350 exhibits the lowest photocatalytic efficiency in *p*-MoO₃/*n*-TiO₂−NF-HJs, ∼70% after reaction for 50 min.

For a better comparison of the photocatalytic efficiency of *p*-MoO₃/*n*-TiO₂−NF-HJs, the kinetic analysis of degradation of RB is conducted as shown in Figure 7(c). The kinetic linear simulation curves over the above catalysts show that the degradation reactions followed a Langmuir−Hinshelwood apparent first-order kinetics model due to the low initial concentrations of RB. The explanation is described below:[36]

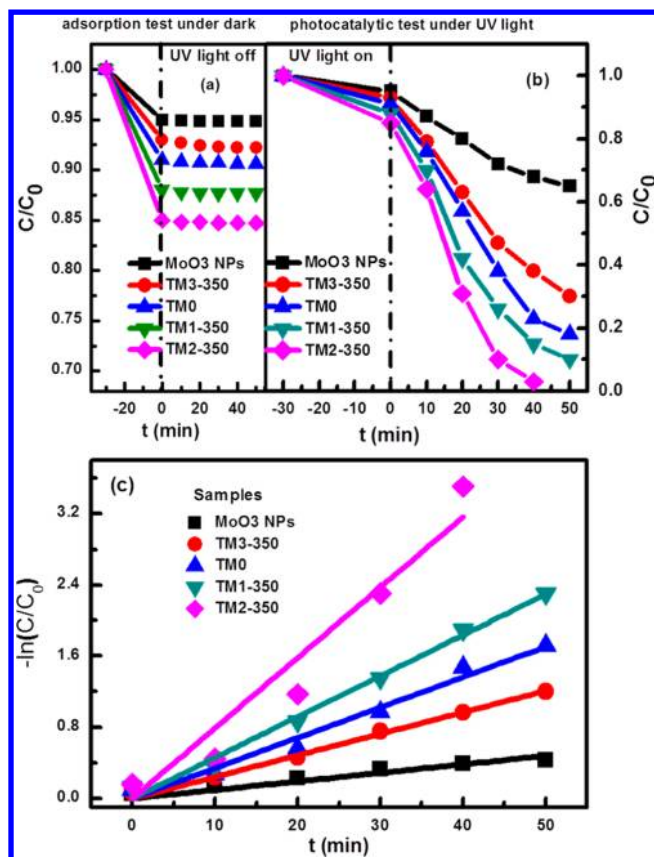$$r = \frac{dC}{dt} = \frac{kKC}{(1 + KC)} \qquad (1)$$

Figure 7. (a) Adsorption of RB over TiO$_2$ nanofibers (TM0), TiO$_2$/MoO$_2$-1, TiO$_2$/MoO$_2$-2, and TiO$_2$/MoO$_2$-3 calcined at 350 °C (denoted as TM1-350, TM2-350, and TM3-350), and MoO$_3$ nanoparticles (MoO$_3$ NPs) under dark; (b) photodegradation of RB over different catalysts against irradiation time under UV light; and (c) kinetic linear fitting curves of RB degradation over different photocatalysts under UV light.

where r is the degradation rate of the reactant (mg/(L·min)), C is the concentration of the reactant (mg/L), t is the UV light irradiation time, k is the reaction rate constant (mg/(L·min)), and K is the adsorption coefficient of the reactant (L/mg). When the initial concentration (C_0) is very low ($C_0 = 10$ mg/L for RB in the present experiment), eq 1 could be simplified to an apparent first-order model:[37]

$$\ln \frac{C_0}{C} = kKt = k_{app}t \qquad (2)$$

where k_{app} is the apparent first-order rate constant (min^{-1}). The determined k_{app} values for degradation of RB with different catalysts are summarized in Table 2.

Given that the active surface areas ($A_{a/s}$) of the different catalysts would affect their activities, normalized k_{app} ($k_{app}/A_{a/s}$) is used to evaluate their photocatalytic activities. We assume the active surface area is proportion to the adsorption of RB, then,

$$A_{a/s} \propto (C_0/C)_{ads} \qquad (3)$$

$$k_{app}/A_{a/s} \propto k_{app} \cdot (C/C_0)_{ads} \qquad (4)$$

The last column in Table 2 shows $k_{app} \cdot (C/C_0)_{ads}$ of different catalysts. It clearly indicates that the normalized k_{app} of TM1-350 and TM2-350 are also much larger than that of TM0 and MoO$_3$ NPs. Notably, the normalized k_{app} of TM2-350 is about twice that of TM0. However, TM3-350 exhibits the lowest

Table 2. Apparent First-Order Rate Constant (Denoted as k_{app}) and Standard Error Obtained by Kinetic Linear Fitting RB Degradation Curves over TiO$_2$ Nanofibers (TM0), TiO$_2$/MoO$_2$-1, TiO$_2$/MoO$_2$-2, and TiO$_2$/MoO$_2$-3 Calcined at 350 °C (Denoted as TM1-350, TM2-350, and TM3-350), and MoO$_3$ Nanoparticles (MoO$_3$ NPs) under UV Light[a]

samples	K_{app} (min^{-1})	standard error	$(C/C_0)_{ads}$	$K_{app} \cdot (C/C_0)_{ads}$ (min^{-1})
MoO3 NP	0.0096	0.0006	0.95	0.009
TM3-350	0.0242	0.0005	0.93	0.023
TM0	0.034	0.001	0.91	0.031
TM1-350	0.046	0.001	0.88	0.040
TM2-350	0.079	0.006	0.85	0.067

[a]$(C/C_0)_{ads}$ represents the adsorption of RB for photocatalysts after 30 min under dark.

normalized k_{app} in p-MoO$_3$/n-TiO$_2$−NF-HJs which is even smaller than that of TM0.

3.5. Photocatalytic Mechanism. To understand the enhancement of the photocatalytic activity of p-MoO$_3$/n-TiO$_2$−HJs, a postulate mechanism is proposed as follows. As shown in Scheme 1(a), the conduction and valence bands of MoO$_3$ are both higher than that of TiO$_2$. When p-type MoO$_3$ and n-type TiO$_2$ contacts forming p−n heterojunctions, electrons transfer from TiO$_2$ to MoO$_3$ while holes transfer from MoO$_3$ to TiO$_2$ until the system attains equilibration between MoO$_3$ and TiO$_2$, as shown in Scheme 1(b). Meanwhile, an internal electric field from TiO$_2$ to MoO$_3$ is built in the interface of MoO$_3$ and TiO$_2$, as confirmed by the XPS results. Under UV light irradiation, both TiO$_2$ and MoO$_3$ could be excited, the generated holes in TiO$_2$ and electrons in MoO$_3$ would be driven to the valence band (VB) of MoO$_3$ and conduction band (CB) of TiO$_2$ by internal electric field, respectively. This transfer process is also thermodynamically favorable because both the CB and VB of MoO$_3$ lie higher than that of TiO$_2$. Therefore, the charge separation of p-MoO$_3$/n-TiO$_2$−NF-HJs would be increased due to the internal electric field and band gap alignment. With increasing loading content of MoO$_3$, the amount of nanoheterojunctions is increased, then, photodegradation efficiencies are improved for TM0, TM1-350 and TM2-350 in sequence. However, because the valence band (VB) of MoO$_3$ is much higher than that of the potential of $E(O_2/H_2O)$ (1.23 V vs NHE), $E(^\bullet OH/OH^-)$ (2.38 V vs NHE) and $E(^\bullet OH/H_2O)$ (2.27 V vs NHE), the oxidation ability of photogenerated holes is very weak. When core/shell structures formed, as illustrated in Scheme 1(c), the photogenerated holes formed on the surface of TM3-350 could not efficiently photodegrade RB. However, photogenerated electrons which play key roles in photocatalytic process for TM1-350 and TM2-350 are collected in the center of TM3-350 and they could not transfer to the surface of the catalyst for photocatalytic reactions due to the internal electric field effect. Therefore, the photocatalytic activity of TM3-350 is decreased.

4. CONCLUSIONS

In summary, novel p-MoO$_3$/n-TiO$_2$−NF-HJs are controllable fabricated by using n-type TiO$_2$ nanofibers via electrospinning and p-type MoO$_3$ nanostructures via hydrothermal and calcinations methods. With increasing the concentration of molybdenum precursor in hydrothermal process, the morphologies of MoO$_3$ are tuned from nanoparticles to nanosheets, and then fully covered shells with increasing their loading on TiO$_2$

nanofibers. The charge separation of p-MoO$_3$/n-TiO$_2$−NF-HJs are enhanced due to the internal electric field of p−n junction effect and band gap alignment, resulting in much higher photocatalytic activities for p-MoO$_3$/n-TiO$_2$−NF-HJs than pure TiO$_2$ nanofibers and MoO$_3$ NPs. Moreover, the core/shell structures of p-MoO$_3$/n-TiO$_2$−NF-HJs with the highest loading of MoO$_3$ could prevent photogenerated electrons from transferring to the surface of the catalysts for photocatalytic reactions due to the internal electric field effect and result in the lowest photocatalytic activity in the p-MoO$_3$/n-TiO$_2$−NF-HJs.

■ AUTHOR INFORMATION

Corresponding Authors
*Tel.: 8643185098803; e-mail: clshao@nenu.edu.cn (C.S.).
*Tel.: 8643185098803; e-mail: lixh781@nenu.edu.cn (X.L.).
Notes
The authors declare no competing financial interest.

■ ACKNOWLEDGMENTS

■ REFERENCES

(1) Hoffmann, M. R.; Martin, S. T.; Choi, W. Y.; Bahnemannt, D. W. Environmental Applications of Semiconductor Photocatalysis. *Chem. Rev.* **1995**, *95*, 69−96.

(2) Bhatkhande, D. S.; Pangarkar, V. G.; Beenackers, A. ACM. Photocatalytic Degradation for Environmental Applications−A Review. *J. Chem. Technol. Biotechnol.* **2001**, *77*, 102−116.

(3) Chong, M. N.; Jin, B.; Chow, C. W. K.; Saint, C. Recent Developments in Photocatalytic Water Treatment Technology: A Review. *Water Res.* **2010**, *44*, 2997−3027.

(4) Zhou, H. L.; Qu, Y. Q.; Zeid, T.; Duan, X. F. Towards Highly Efficient Photocatalysts Using Semiconductor Nanoarchitectures. *Energy Environ. Sci.* **2012**, *5*, 6732−6743.

(5) Chai, S. Y.; Kim, Y. J.; Jung, M. H.; Chakraborty, A. K.; Jung, D.; Lee, W. I. Heterojunctioned BiOCl/Bi$_2$O$_3$, A New Visible Light Photocatalyst. *J. Catal.* **2009**, *262*, 144−149.

(6) Zhang, L.; Wong, K. H.; Chen, Z.; Yu, J. C.; Zhao, J.; Hu, C.; Chan, C. Y.; Wong, P. K. AgBr−Ag−Bi$_2$WO$_6$ Nanojunction System: A Novel and Efficient Photocatalyst with Double Visible-Light Active Components. *Appl. Catal., A* **2009**, *363*, 221−229.

(7) Xie, B. P.; Zhang, H. X.; Cai, P. X.; Qiu, R. L.; Xiong, Y. Simultaneous Photocatalytic Reduction of Cr(VI) and Oxidation of Phenol over Monoclinic BiVO$_4$ under Visible Light Irradiation. *Chemosphere* **2006**, *63*, 956−963.

(8) Linsebigler, A. L.; Lu, G.; Yates, J. T. Photocatalysis on TiO$_2$ Surfaces: Principles, Mechanisms, and Selected Results. *Chem. Rev.* **1995**, *95*, 735−758.

(9) Fujishima, A.; Zhang, X. T.; Tryk, D. A. TiO$_2$ Photocatalysis and Related Surface Phenomena. *Surf. Sci. Rep.* **2008**, *63*, 515−582.

(10) Gaya, U. I.; Abdullah, A. H. Heterogeneous Photocatalytic Degradation of Organic Contaminants over Titanium Dioxide: A Review of Fundamentals, Progress and Problems. *J. Photochem. Photobiol., C* **2008**, *9*, 1−12.

(11) Liu, Z. Y.; Sun, D. D.; Guo, P.; Leckie, J. O. An Efficient Bicomponent TiO$_2$/SnO$_2$ Nanofiber Photocatalyst Fabricated by Electrospinning with A Side-by-Side Dual Spinneret Method. *Nano Lett.* **2007**, *7*, 1081−1085.

(12) Yang, H. Y.; Yu, S. F.; Lau, S. P.; Zhang, X. W.; Sun, D. D.; Jun, G. Direct Growth of ZnO Nanocrystals onto the Surface of Porous TiO$_2$ Nanotube Arrays for Highly Efficient and Recyclable Photocatalysts. *Small* **2009**, *5*, 2260−2264.

(13) Zhang, M. Y.; Shao, C. L.; Mu, J. B.; Zhang, Z. Y.; Guo, Z. C.; Zhang, P.; Liu, Y. C. One-Dimensional Bi$_2$MoO$_6$/TiO$_2$ Hierarchical Heterostructures with Enhanced Photocatalytic Activity. *CrystEngComm* **2012**, *14*, 605−612.

(14) Zhang, Z. Y.; Shao, C. L.; Li, X. H.; Wang, C. H.; Zhang, M. Y.; Liu, Y. C. Electrospun Nanofibers of p-Type NiO/n-Type ZnO Heterojunctions with Enhanced Photocatalytic Activity. *ACS Appl. Mater. Interfaces* **2010**, *2*, 2915−2923.

(15) Sarkar, D.; Ghosh, C. K.; Mukherjee, S.; Chattopadhyay, K. K. Three Dimensional Ag$_2$O/TiO$_2$ Type-II (p−n) Nanoheterojunctions for Superior Photocatalytic Activity. *ACS Appl. Mater. Interfaces* **2013**, *5*, 331−337.

(16) Yu, J. G.; Wang, W. G.; Cheng, B. Synthesis and Enhanced Photocatalytic Activity of a Hierarchical Porous Flowerlike p−n Junction NiO/TiO$_2$ Photocatalyst. *Chem.—Asian J.* **2010**, *5*, 2499−2506.

(17) Yang, L.; Luo, S.; Li, Y.; Xiao, Y.; Kang, Q.; Cai, Q. High Efficient Photocatalytic Degradation of p-Nitrophenol on a Unique Cu$_2$O/TiO$_2$ p−n Heterojunction Network Catalyst. *Environ. Sci. Technol.* **2010**, *44*, 7641−7646.

(18) Chen, S. F.; Zhang, S. J.; Liu, W.; Zhao, W. Preparation and Activity Evaluation of p−n Junction Photocatalyst NiO/TiO$_2$. *J. Hazard. Mater.* **2008**, *155*, 320−326.

(19) Chen, S. F.; Zhao, W.; Liu, W.; Zhang, S. J. Preparation,Characterization and Activity Evaluation of p−n Junction Photocatalyst p-ZnO/n-TiO$_2$. *Appl. Surf. Sci.* **2008**, *255*, 2478−2484.

(20) Zhao, D. W.; Sun, X. W.; Jiang, C. Y.; Kyaw, A. K. K.; Lo, G. Q.; Kwong, D. L. Efficient Tandem Organic Solar Cells with An Al/MoO$_3$ Intermediate Layer. *Appl. Phys. Lett.* **2008**, *93*, 083305.

(21) Hamwi, S.; Meyer, J.; Winkler, T.; Riedl, T.; Kowalsky, W. p-Type Doping Efficiency of MoO$_3$ in Organic Hole Transport Materials. *Appl. Phys. Lett.* **2009**, *94*, 253307.

(22) Kyaw, A. K. K.; Sun, X. W.; Jiang, C. Y.; Lo, G. Q.; Zhao, D. W.; Kwong, D. L. An Inverted Organic Solar Cell Employing A Sol-Gel Derived ZnO Electron Selective Layer and Thermal Evaporated MoO$_3$ Hole Selective Layer. *Appl. Phys. Lett.* **2008**, *93*, 221107.

(23) Lianos, P. Production of Electricity and Hydrogen by Photocatalytic Degradation of Organic Wastes in A Photoelectrochemical Cell-The Concept of The Photofuelcell: A Review of a Re-emerging Research Field. *J. Hazard. Mater.* **2011**, *185*, 575−590.

(24) Tchatchueng, J. B.; Loura, B. B.; Atchana, J.; Kamga, R. TiO$_2$—MoO$_3$ as Photocatalyst for Azo and Triphenylmethane Dyes Decolouration. *J. Environ. Sci. Technol.* **2009**, *2*, 31−39.

(25) Natori, H.; Kobayashi, K.; Takahashi, M. Fabrication and Photocatalytic Activity of TiO$_2$/MoO$_3$ Particulate Films. *J. Oleo Sci.* **2009**, *58*, 203−211.

(26) Kong, F.; Huang, L.; Luo, L.; Chu, S.; Wang, Y.; Zou, Z. Synthesis and Characterization of Visible Light Driven Mesoporous Nano-Photocatalyst MoO$_3$/TiO$_2$. *J. Nanosci. Nanotechnol.* **2012**, *12*, 1931−1937.

(27) Agarwal, P.; Paramasivam, I.; Shrestha, N. K.; Schmuki, P. MoO$_3$ in Self-Organized TiO$_2$ Nanotubes for Enhanced Photocatalytic Activity. *Chem.—Asian J.* **2010**, *5*, 66−69.

(28) Zhang, Z.; Shao, C.; Li, X.; Sun, Y.; Zhang, M.; Mu, J.; Zhang, P.; Guo, Z.; Liu, Y. Hierarchical Assembly of Ultrathin Hexagonal SnS$_2$ Nanosheets onto Electrospun TiO$_2$ Nanofibers: Enhanced Photocatalytic Activity Based on Photoinduced Interfacial Charge Transfer. *Nanoscale* **2013**, *5*, 606−618.

(29) Zhang, X.; Li, X.; Shao, C.; Li, J.; Zhang, M.; Zhang, P.; Wang, K.; Lu, N.; Liu, Y. One-Dimensional Hierarchical Heterostructures of In$_2$S$_3$ Nanosheets on Electrospun TiO$_2$ Nanofibers with Enhanced Visible Photocatalytic Activity. *J. Hazard. Mater.* **2013**, *260*, 892−900.

(30) Zhang, P.; Shao, C.; Zhang, Z.; Zhang, M.; Mu, J.; Guo, Z.; Liu, Y. In Situ Assembly of Well-Dispersed Ag Nanoparticles (AgNPs) on Electrospun Carbon Nanofibers (CNFs) for Catalytic Reduction of 4-nitrophenol. *Nanoscale* **2011**, *3*, 3357−3363.

(31) Cao, T.; Li, Y.; Wang, C.; Shao, C.; Liu, Y. A Facile in Situ Hydrothermal Method to SrTiO$_3$/TiO$_2$ Nanofiber Heterostructures with High Photocatalytic Activity. *Langmuir* **2011**, *27*, 2946−2952.

(32) Choi, J. G.; Thompson, L. T. XPS Study of As-Prepared and Reduced Molybdenum Oxides. *Appl. Surf. Sci.* **1996**, *93*, 143−149.

(33) Chen, Z. Y.; Santoso, I.; Wang, R.; Xie, L. F.; Mao, H. Y.; Huang, H.; Wang, Y. Z.; Gao, X. Y.; Chen, Z. K.; Ma, D. G.; Wee, A. T. S.; Chen, W. Surface Transfer Hole Doping of Epitaxial Graphene Using MoO$_3$ Thin Film. *Appl. Phys. Lett.* **2010**, *96*, 213104.

(34) Wang, C. H.; Shao, C. L.; Zhang, X. T.; Liu, Y. C. SnO$_2$ Nanostructures−TiO$_2$ Nanofibers Heterostructures: Controlled Fabrication and High Photocatalytic Properties. *Inorg. Chem.* **2009**, *48*, 7261−7268.

(35) Zhang, Z. Y.; Shao, C. L.; Zhang, L. N.; Li, X. H.; Liu, Y. C. Electrospun Nanofibers of V-Doped TiO$_2$ with High Photocatalytic Activity. *J. Colloid Interface Sci.* **2010**, *351*, 57−62.

(36) Turchi, C. S.; Ollis, D. F. J. Photocatalytic Degradation of Organic Water Contaminants: Mechanisms Involving Hydroxyl Radical Attack. *J. Catal.* **1990**, *122*, 178−192.

(37) Lee, M. S.; Park, S. S.; Lee, G. D.; Ju, C. S.; Hong, S. S. Synthesis of TiO$_2$ Particles by Reverse Microemulsion Method Using Nonionic Surfactants with Different Hydrophilic and Hydrophobic Group and Their Photocatalytic Activity. *Catal. Today* **2005**, *101*, 283−290.